As observed in FMO, coherences between singly excited electronic states persist longer than the coherences between the ground state and the individual excited states by an order of magnitude (*28*), suggesting that the energetic fluctuations responsible for dephasing each exciton are correlated.

A similar pattern is observed in the power spectrum of the trace taken from the spectra of dimer AC. Here, the prominent 693 cm^{-1} peak in the transform is absent from the transform from the control experiments. Although a nearby feature appears in the power spectrum from the corresponding mixture of monomers (fig. S4), this feature is below the noise floor of the transform, which we define as 1.5 times the mean value of the spectrum. The energy gap inferred from the monomers A′ and C′ absorption maxima is 705 cm^{-1} (Fig. 4, solid magenta line), which again is in excellent agreement with the beat frequency observed in the 2D spectra. This method of estimating the energy gap between excited states inherently neglects any shifts that may occur because of coupling between electronic states. The fit to this trace gives a frequency of 703 ± 10 cm^{-1}, and the dephasing time obtained from the linewidth of the peak in the power spectrum is 60 fs. Last, the power spectrum of dimer BC shows a strong peak at 199 cm^{-1}, which the fit to the trace refines to 195 ± 4 cm^{-1}, again matching the inferred energy gap of 201 cm^{-1}. The dephasing time for this peak is also 60 fs.

The time traces of the off-diagonal features in the spectra of the dimers exhibit oscillatory behavior associated with coherent evolution at frequencies corresponding to the respective transition energy gaps, whereas traces taken at identical spectral coordinates in the spectra of the corresponding monomers demonstrate only vibrational oscillations. This disparity allows us to assign these quantum beats to coherences between the electronic excited states of the dimers. The synthetic ease with which we control the energy gap between the monomers allows us to follow the frequency of the beating signal between three different dimers, further demonstrating the electronic nature of these oscillations.

By replicating in a simple synthetic system the long-lived electronic coherence observed in biological systems, we confirm the generality of this phenomenon and introduce a framework for dissecting the complex information contained in 2D spectra of natural multichromophoric systems. In creating the first model system for such effects, we have identified that proximity, fixed orientation, and electronic coupling are sufficient to support persistent coherence. This system will allow complementary experimental and theoretical approaches to fully understand the role of quantum coherence in chemical dynamics. Furthermore, this work lays the groundwork for the development of artificial energy-transfer devices that exploit the improved transfer efficiency obtained from the synergy between coherent and incoherent dynamics.

References and Notes

1. G. S. Engel *et al.*, *Nature* **446**, 782 (2007).
2. T. R. Calhoun *et al.*, *J. Phys. Chem. B* **113**, 16291 (2009).
3. E. Collini *et al.*, *Nature* **463**, 644 (2010).
4. E. Harel, G. S. Engel, *Proc. Natl. Acad. Sci. U.S.A.* **109**, 706 (2012).
5. G. Panitchayangkoon *et al.*, *Proc. Natl. Acad. Sci. U.S.A.* **107**, 12766 (2010).
6. D. Hayes, J. Wen, G. Panitchayangkoon, R. E. Blankenship, G. S. Engel, *Faraday Discuss.* **150**, 459, discussion 505 (2011).
7. N. Christensson *et al.*, *J. Phys. Chem. B* **115**, 5383 (2011).
8. F. Caycedo-Soler, A. W. Chin, J. Almeida, S. F. Huelga, M. B. Plenio, *J. Chem. Phys.* **136**, 155102 (2012).
9. N. Christensson, H. F. Kauffmann, T. Pullerits, T. Mančal, *J. Phys. Chem. B* **116**, 7449 (2012).
10. V. Tiwari, W. K. Peters, D. M. Jonas, *Proc. Natl. Acad. Sci. U.S.A.* **110**, 1203 (2013).
11. H. Lee, Y. C. Cheng, G. R. Fleming, *Science* **316**, 1462 (2007).
12. G. Panitchayangkoon *et al.*, *Proc. Natl. Acad. Sci. U.S.A.* **108**, 20908 (2011).
13. G. S. Engel, *Procedia Chem.* **3**, 222 (2011).
14. E. W. Knapp, *Chem. Phys.* **85**, 73 (1984).
15. V. Balevičius Jr., A. Gelzinis, D. Abramavicius, T. Mančal, L. Valkunas, *Chem. Phys.* **404**, 94 (2012).
16. F. Milota, J. Sperling, A. Nemeth, T. Mančal, H. F. Kauffmann, *Acc. Chem. Res.* **42**, 1364 (2009).
17. O. Bixner *et al.*, *J. Chem. Phys.* **136**, 204503 (2012).
18. B. S. Prall, D. Y. Parkinson, N. Ishikawa, G. R. Fleming, *J. Phys. Chem. A* **109**, 10870 (2005).
19. S. Cho *et al.*, *J. Phys. Chem. A* **115**, 3990 (2011).
20. A. Ishizaki, G. R. Fleming, *J. Chem. Phys.* **130**, 234110 (2009).
21. G. K. Walkup, S. C. Burdette, S. J. Lippard, R. Y. Tsien, *J. Am. Chem. Soc.* **122**, 5644 (2000).
22. W.-C. Sun, K. R. Gee, D. H. Klaubert, R. P. Haugland, *J. Org. Chem.* **62**, 6469 (1997).
23. I. L. Arbeloa, *J Chem Soc Farad T 2* **77**, 1725 (1981).
24. Y. C. Cheng, G. S. Engel, G. R. Fleming, *Chem. Phys.* **341**, 285 (2007).
25. T. Brixner, T. Mančal, I. V. Stiopkin, G. R. Fleming, *J. Chem. Phys.* **121**, 4221 (2004).
26. M. L. Cowan, J. P. Ogilvie, R. J. D. Miller, *Chem. Phys. Lett.* **386**, 184 (2004).
27. J. D. Hybl, A. A. Ferro, D. M. Jonas, *J. Chem. Phys.* **115**, 6606 (2001).
28. D. Hayes *et al.*, *New J. Phys.* **12**, 065042 (2010).
29. J. R. Caram, A. F. Fidler, G. S. Engel, *J. Chem. Phys.* **137**, 024507 (2012).
30. R. W. Wood, G. Collins, *Phys. Rev.* **42**, 386 (1932).

Acknowledgments: Details of the synthesis, spectroscopy, and data analysis are included in the supplementary materials. The authors would like to thank the NSF Materials Research and Engineering Center (grant DMR 08-02054), Air Force Office of Scientific Research (grant FA9550-09-1-0117), Defense Threat Reduction Agency (HDTRA1-10-1-0091 P00002), the Defense Advanced Research Projects Agency QuBE program (grant N66001-10-1-4060), and the Searle Foundation for supporting this work. D.H. thanks the NSF Graduate Research Fellowship Program program for funding. The mass spectrometry facility used for this work is supported by NSF grant CHE-1048528. The authors gratefully acknowledge the experimental efforts of R. McGillicuddy, P. Dahlberg, K. A. Fransted, T. Jarvis, and C. J. Qin and thank S. Viswanathan and A. Fidler for useful discussions.

Supplementary Materials

www.sciencemag.org/cgi/content/full/science.1233828/DC1
Materials and Methods
Figs. S1 to S5
References (*31*–*33*)

10 December 2012; accepted 2 April 2013
Published online 18 April 2013;
10.1126/science.1233828

Direct Imaging of Covalent Bond Structure in Single-Molecule Chemical Reactions

Dimas G. de Oteyza,[1,2]* Patrick Gorman,[3]* Yen-Chia Chen,[1,4]* Sebastian Wickenburg,[1,4] Alexander Riss,[1] Duncan J. Mowbray,[5,6] Grisha Etkin,[3] Zahra Pedramrazi,[1] Hsin-Zon Tsai,[1] Angel Rubio,[2,5,6] Michael F. Crommie,[1,4]† Felix R. Fischer[3,4]†

Observing the intricate chemical transformation of an individual molecule as it undergoes a complex reaction is a long-standing challenge in molecular imaging. Advances in scanning probe microscopy now provide the tools to visualize not only the frontier orbitals of chemical reaction partners and products, but their internal covalent bond configurations as well. We used noncontact atomic force microscopy to investigate reaction-induced changes in the detailed internal bond structure of individual oligo-(phenylene-1,2-ethynylenes) on a (100) oriented silver surface as they underwent a series of cyclization processes. Our images reveal the complex surface reaction mechanisms underlying thermally induced cyclization cascades of enediynes. Calculations using ab initio density functional theory provide additional support for the proposed reaction pathways.

Understanding the microscopic rearrangements of matter that occur during chemical reactions is of great importance for catalytic mechanisms and may lead to greater efficiencies in industrially relevant processes (*1*, *2*). However, traditional chemical structure characterization methods are typically limited to ensemble techniques where different molecular structures, if present, are convolved in each measurement (*3*). This limitation complicates the determination of final chemical products, and often it renders such identification impossible for products present only in small amounts. Single-molecule characterization techniques such as scanning tun-

tween the monomers, but even at cryogenic temperature, the exciton peaks are not individually resolved, indicating that the coupling is weak. The absorption spectra of monomers A′, B′, and C′ (fig. S1) were used to approximate the energies of the electronic transitions in the dimers, giving 524.1, 538.3, and 544.2 nm, respectively. The shapes of these spectra further confirm that intermolecular dimers and trimers are not present in significant concentrations.

Two-dimensional electronic spectroscopy has been used to observe quantum beats arising from electronic coherences and quantify their dephasing rates in a number of photosynthetic antenna complexes, including the FMO complex (*1*), phycobiliproteins (*3*), light-harvesting complex 2 (LH2) (*4*), and LHCII (*2*). This method is particularly suited to such experiments because it separates signals arising from coherences into specific, predictable locations in a frequency-frequency spectrum (*24*). In this four-wave mixing technique, which has been thoroughly described elsewhere (*25*–*27*), a pair of phase-locked, ultrashort laser pulses interacts with the sample, yielding a population state or a coherence between singly excited states. The system is allowed to evolve for a time T (the waiting time) before a third pulse interacts with the sample, resulting in the emission of the third-order signal. The 2D spectra presented here can be considered to plot "energy in" along the coherence frequency axis (ω_τ, horizontal axis) and "energy out" along the rephasing frequency axis (ω_t, vertical axis). Phase-matching considerations dictate the use of negative coherence frequencies ("$-\omega_\tau$" rather than "ω_τ"). A series of 2D spectra taken at different waiting times gives ultrafast temporal resolution of spectral features, revealing both incoherent (exponential) relaxation dynamics and coherent (oscillatory) evolution in peak shapes and amplitudes. The lifetime of coherences can then be measured as the damping rate of such oscillatory signals (*28*).

Series of 2D spectra were acquired at waiting times $T = 50$ to 1000 fs in steps of 10 fs for each dimer. Control experiments were also performed with monomers A′, B′, and C′ individually; equimolar mixtures of pairs of monomers A′, B′, and C′; a homodimer (dimer BB); and a solvent blank. Absolute value 2D spectra for each heterodimer taken at $T = 200$ fs are shown in Fig. 3, whereas spectra of the mixtures of monomers are shown in fig. S2. The features in the $T = 200$ fs spectra of the dimers are significantly broader along $-\omega_\tau$ than their respective linear absorption spectra as a result of fast relaxation during the coherence time. The majority of the signal appears well below the diagonal, due in part to this fast Stokes shift occurring during early waiting times. Perhaps more important, however, is the spectral position of the laser pulse, which is centered near the emission frequencies of the dimers (Fig. 2) with substantial bandwidth extending further into the red, favoring stimulated emission to vibrationally excited states within the electronic ground state manifold (*29*). In 2D electronic spectroscopy, we detect only signals within our laser bandwidth, so overlapping with both the absorption and emission spectra ensures that we retain a signal throughout the Stokes shift.

Time traces for each dimer were taken by integrating the absolute value signal over a 30 by 30 cm^{-1} square centered at a value of ω_τ equal to the absorption maximum of the higher-energy aminoalkylated monomer and at a value of ω_t equal to the absorption maximum of the lower-energy monomer. For comparison, traces were taken from the spectra of the corresponding equimolar mixtures of monomers (monomers A′ and B′ for dimer AB, monomers A′ and C′ for dimer AC, and monomers B′ and C′ for dimer BC) at the same spectral locations. Each trace was fit to the sum of two exponential decays, and Fourier transforms of the apodized residuals are plotted in Fig. 4. These power spectra show the relative contributions of the frequencies that produce the beating found in these traces. Although ethanol has a strong Raman mode at 883 cm^{-1} (*30*), this frequency is observed only in the spectra of the solvent blank, demonstrating that the resonant signal from all samples overwhelms the nonresonant solvent contribution in these experiments. Thus, the frequencies shown in Fig. 4 arise exclusively from the vibrational and electronic coherences of the dimers.

To facilitate assignment of peaks in these power spectra, the same analysis was performed on the spectra of the monomers (fig. S3). Between 150 and 1000 cm^{-1}, strong peaks were found at 275, 342, and 410 cm^{-1} in monomer A′; 342, 414, 581, and 737 cm^{-1} in monomer B′; and 175, 290, 573, and 750 cm^{-1} in monomer C′ (the higher frequency peaks in the monomer spectra are not included for the sake of simplicity). These frequencies are indicated with dashed lines in Fig. 4, accounting for all but one of the frequencies observed in the spectra of the dimers. Because these peaks are all present in single-chromophore spectra, they are assigned to the vibrational modes of their respective monomers. These frequencies also account for most of the peaks observed in the generally noisy spectra of the mixtures of monomers (fig. S4).

An additional peak in the power spectrum of the trace taken from the spectra of dimer AB that is not present in the mixture of monomers A′ and B′ appears at 500 cm^{-1}. This result is consistent across three data sets acquired on different days with slightly different laser pulses. A least-squares fit of the residual trace to the sum of five damped sinusoids (fig. S5) gives a frequency of 499 ± 8 cm^{-1}. This frequency is in excellent agreement with the 503 cm^{-1} difference between the absorption maxima of monomers A′ and B′ (Fig. 4, solid blue line), as is expected for a beat arising from electronic coherence within the dimer. Because of the large number of fitting parameters, however, the error in the dephasing time obtained from this fit is greater than the dephasing time itself. Therefore, an approximate dephasing time of 90 fs was obtained from the linewidth of the peak in the power spectrum, which because of the apodization process represents a lower bound. In contrast, for a fixed waiting time the signal decays completely within 40 fs of coherence time, giving a dephasing (*e*-folding) time of less than 15 fs for coherences between the ground state and the individual excited states.

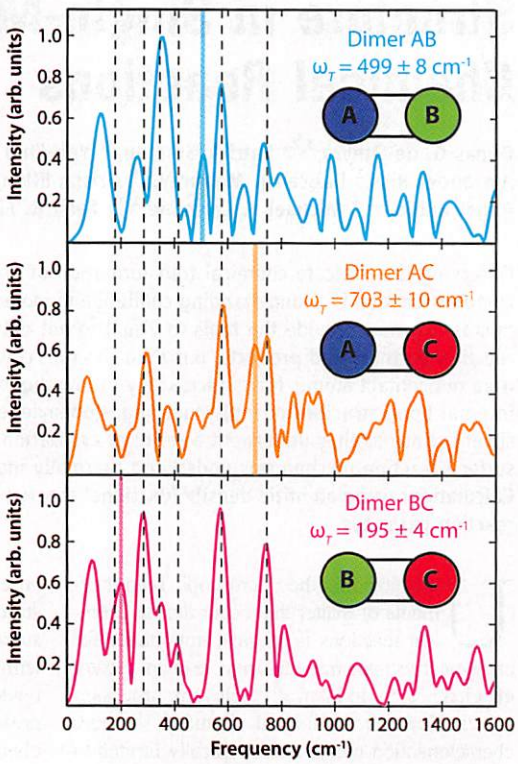

Fig. 4. Power spectra of cross peak oscillations reveal persistent electronic coherence. Fourier transforms of waiting-time traces were taken from the lower crosspeaks of the 2D spectra of dimers AB (**top**), AC (**middle**), and BC (**bottom**). The energy gaps between the absorption maxima of the aminoalkylated monomers are shown as solid colored lines (monomers A′ and B′, blue; monomers A′ and C′, orange; monomers B′ and C′, magenta), whereas peaks assigned to vibrational coherences are indicated with dashed black lines.

neling microscopy (STM) (*4*, *5*) potentially provide a means for surpassing these limitations. Structural identification using STM, however, is limited by the microscopic contrast arising from the electronic local density of states (LDOS), which is not always easily related to chemical structure. Another important subnanometer-resolved technique is transmission electron microscopy (TEM). Here, however, the high-energy electron beam is often too destructive for organic molecule imaging. Recent advances in tuning fork–based noncontact atomic force microscopy (nc-AFM) provide a method capable of nondestructive subnanometer spatial resolution (*6*–*10*). Single-molecule images obtained with this technique are reminiscent of wire-frame chemical structures and even allow differences in chemical bond order to be identified (*10*). Here we show that it is possible to resolve with nc-AFM the intramolecular structural changes and bond rearrangements associated with complex surface-supported cyclization cascades, thereby revealing the microscopic processes involved in chemical reaction pathways.

Intramolecular structural characterization was performed on the products of a thermally induced enediyne cyclization of 1,2-bis((2-ethynylphenyl) ethynyl)benzene (**1**). Enediynes exhibit a variety of radical cyclization processes known to compete with traditional Bergman cyclizations (*11*, *12*), thus often rendering numerous products with complex structures that are difficult to characterize using ensemble techniques (*13*). To directly image these products with subnanometer spatial resolution, we thermally activated the cyclization reaction on an atomically clean metallic surface under ultrahigh vacuum (UHV). We used STM and nc-AFM to probe both the reactant and final products at the single-molecule level. Our images reveal how the thermally induced complex bond rearrangement of **1** resulted in a variety of unexpected products, from which we have obtained a detailed mechanistic picture—corroborated by ab initio density functional theory (DFT) calculations—of the cyclization processes.

We synthesized 1,2-bis((2-ethynylphenyl)ethynyl) benzene (**1**) through iterative Sonogashira cross-coupling reactions (scheme S1) (*14*). We deposited **1** from a Knudsen cell onto a Ag(100) surface held at room temperature under UHV. Molecule-decorated samples were transferred to a cryogenic imaging stage ($T \leq 7$ K) before and after undergoing a thermal annealing step. Cryogenic imaging was performed both in a home-built $T = 7$ K scanning tunneling microscope and in a qPlus-equipped (*15*, *16*) commercial Omicron LT-STM/AFM at $T = 4$ K. nc-AFM images were recorded by measuring the frequency shift of the qPlus resonator while scanning over the sample surface in constant-height mode. For nc-AFM measurements, the apex of the tip was first functionalized with a single CO molecule (*6*). To assess the reaction pathway energetics, we performed ab initio DFT calculations within the local density approximation (*17*) using the GPAW (Grid-based Projector Augmented Wavefunction) code (*18*, *19*).

Figure 1A shows a representative STM image of **1** on Ag(100) before undergoing thermal annealing. The adsorbed molecules each exhibited three maxima in their LDOS at positions suggestive of the phenyl rings in **1** (Fig. 1A). Annealing the molecule-decorated Ag surface up to 80°C left the structure of the molecules unchanged. Annealing the sample at $T \geq 90$°C, however, induced a chemical transformation of **1** into distinctively different molecular products (some molecular desorption was observed). Figure 1B shows an STM image of the surface after annealing at 145°C for 1 min. Two of the reaction products can be seen in this image, labeled as **2** and **3**. The structures of the products are unambiguously distinguishable from one another and from the starting material **1**, as shown in the close-up STM images of the most common products **2**, **3**, and **4** in Fig. 2, B to D. The observed product ratios are **2**:**3**:**4** = (51 ± 7%):(28 ± 5%):(7 ± 3%), with the remaining products comprising other minority monomers as well as fused oligomers (fig. S2) (*14*).

Detailed subnanometer-resolved structure and bond conformations of the molecular reactant **1** and products (**2**, **3**, and **4**) were obtained by performing nc-AFM measurements of the molecule-decorated sample both before and after annealing at $T \geq 90$°C. Figure 2E shows a nc-AFM image of **1** before annealing. In contrast to the STM image (Fig. 2A) of **1**, which reflects the diffuse electronic LDOS of the molecule, the AFM image reveals the highly spatially resolved internal bond structure. A dark halo observed along the periphery of the molecule is associated with long-range electrostatic and van der Waals interactions (*6*, *20*). The detailed intramolecular contrast arises from short-ranged Pauli repulsion, which is maximized in the regions of highest electron density (*20*). These regions include the atomic positions and the covalent bonds. Even subtle differences in the electron density attributed to specific bond orders can be distinguished (*10*), as evidenced by the enhanced contrast at the positions of the triple bonds within **1**. This effect is to be distinguished from the enhanced contrast observed along the periphery of the molecule, where spurious effects (e.g., because of a smaller van der Waals background, enhanced electron density at the boundaries of the delocalized π-electron system, and molecular deviations from planarity) generally influence the contrast (*10*, *20*).

Figure 2, F to H, shows subnanometer-resolved nc-AFM images of reaction products **2**, **3**, and **4** that were observed after annealing the sample at $T > 90$°C. The structure of these products remained unaltered even after further annealing to temperatures within the probed range from 90° to 150°C (150°C was the maximum annealing temperature explored in this study). The nc-AFM images reveal structural patterns of annulated six-, five-, and four-membered rings. The inferred molecular structures are shown in Fig. 2, J to L. Internal bond lengths measured by nc-AFM have previously been shown to correlate with Pauling bond order (*10*), but with deviations occurring near a molecule's periphery, as described above. As a result, we could extract clear bonding geometries for the products (Fig. 2, J to L), but not their detailed bond order. The subtle radial streaking extending from the peripheral carbon atoms suggests that the valences of the carbon atoms are terminated by hydrogen (*20*). This is in agreement with molecular mass conservation for all proposed product structures and indicates that the chemical reactions leading to products **2**, **3**, and **4** are exclusively isomerization processes (*21*).

Our ability to directly visualize the bond geometry of the reaction products (Fig. 2, F to H)

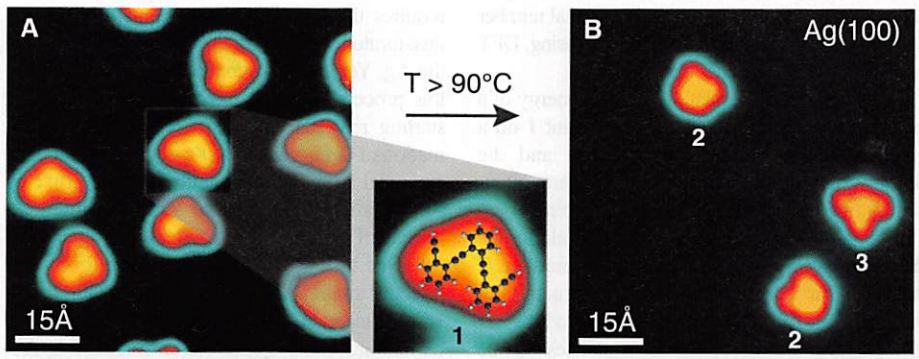

Fig. 1. STM images of a reactant-decorated Ag(100) surface before and after thermally induced cyclization reactions. (A) Constant-current STM image of **1** as deposited on Ag(100) ($I = 25$ pA, $V = 0.1$ V, $T = 7$ K). A model of the molecular structure is overlaid on a close-up STM image. **(B)** STM image of products **2** and **3** on the surface shown in (A) after annealing at $T = 145$°C for 1 min ($I = 45$ pA, $V = 0.1$ V, $T = 7$ K).

[1]Department of Physics, University of California, Berkeley, CA 94720, USA. [2]Centro de Física de Materiales CSIC/UPV-EHU-Materials Physics Center, Paseo Manuel de Lardizabal 5, E-20018 San Sebastián, Spain. [3]Department of Chemistry, University of California, Berkeley, CA 94720, USA. [4]Materials Sciences Division, Lawrence Berkeley National Laboratory, Berkeley, CA 94720, USA. [5]Donostia International Physics Center, Paseo Manuel de Lardizabal 4, E-20018 San Sebastián, Spain. [6]Nano-Bio Spectroscopy Group and ETSF Scientific Development Center, Dpto. de Física de Materiales, Universidad del País Vasco UPV/EHU, Avenida de Tolosa 72, E-20018 San Sebastián, Spain.

*These authors contributed equally to this work.
†Corresponding author. E-mail: crommie@berkeley.edu (M.F.C.); ffischer@berkeley.edu (F.R.F.)

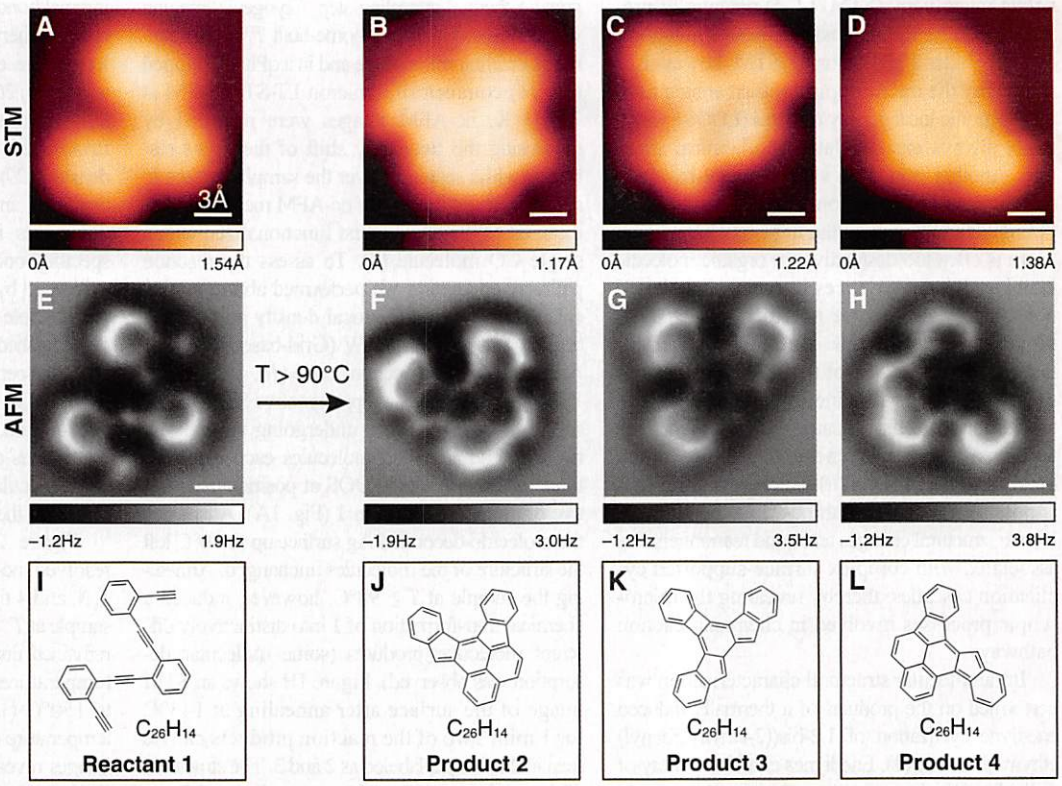

Fig. 2. Comparison of STM images, nc-AFM images, and structures for molecular reactant and products. (**A**) STM image of **1** on Ag(100) before annealing. (**B** to **D**) STM images of individual products **2**, **3**, and **4** on Ag(100) after annealing at $T > 90°C$ ($I = 10$ pA, $V = -0.2$ V, $T = 4$ K). (**E**) nc-AFM image of the same molecule (reactant **1**) depicted in (A). (**F** to **H**) nc-AFM images of the same molecules (products **2**, **3**, and **4**) depicted in (B) to (D). nc-AFM images were obtained at sample bias $V = -0.2$ V (qPlus sensor resonance frequency = 29.73 kHz, nominal spring constant = 1800 N/m, Q-value = 90,000, oscillation amplitude = 60 pm). (**I** to **L**) Schematic representation of the molecular structure of reactant **1** and products **2**, **3**, and **4**. All images were acquired with a CO-modified tip.

provides insight into the detailed thermal reaction mechanisms that convert **1** into the products. We limit our discussion to the reaction pathways leading from **1** to the two most abundant products, **2** and **3**. The reactivity of *oligo*-1,2-diethynylbenzene **1** can be rationalized by treating the 1,2-diethynylbenzene subunits as independent but overlapping enediyne systems that are either substituted by two phenyl rings for the central enediyne, or by one phenyl ring and one hydrogen atom in the terminal segments. This treatment suggests three potential cyclizations along the reaction pathway (resulting in six-, five-, or four-membered rings) (*22*), in addition to other possible isomerization processes such as [1,2]-radical shifts or bond rotations that have been observed in related systems (*23*). Combinations of these processes leading to the products in a minimal number of steps were explored and analyzed using DFT calculations (*14*).

We started by calculating the total energy of a single adsorbed molecule of the reactant **1** on a Ag(100) surface. Activation barriers and the energy of metastable intermediates were calculated (including molecule-surface interactions) for a variety of isomeric structures along the reaction pathway leading toward the products **2** and **3**. Our observations that the structure of reactants on Ag(100) remains unchanged for $T <$ 90°C and that no reaction intermediates can be detected among the products indicate that the initial enediyne cyclization is associated with a notable activation barrier that represents the rate-determining step in the reaction. In agreement with experiments, DFT calculations predict an initial high barrier for the first cyclization reactions, followed by a series of lower barriers associated with subsequent bond rotations and hydrogen shifts.

Figure 3A shows the reaction pathway determined for the transformation of **1** into product **2**. The rate-determining activation barrier is associated with a C^1–C^6 Bergman cyclization of a terminal enediyne coupled with a C^1–C^5 cyclization of the internal enediyne segment to give the intermediate diradical **Int1** in an overall exothermic process (–60.8 kcal mol^{-1}). Rotation of the third enediyne subunit around a double bond, followed by the C^1–C^5 cyclization of the fulvene radical with the remaining triple bond, leads to **Int2**. The rotation around the exocyclic double bond is hindered by the Ag surface and requires the breaking of the bond between the unsaturated valence on the sp^2 carbon atom and the Ag. Yet the activation barrier associated with this process does not exceed the energy of the starting material used as a reference. The formation of three new carbon-carbon bonds and the extended aromatic conjugation stabilize **Int2** by –123.9 kcal mol^{-1} relative to **1**. Finally, a sequence of radical [1,2]- and [1,3]-hydrogen shifts followed by a C^1–C^6 cyclization leads from **Int2** directly to the dibenzofulvalene **2**. Our calculations indicate that the substantial activation barriers generally associated with radical hydrogen shifts in the gas phase (50 to 60 kcal mol^{-1}) (*24*, *25*) are lowered through the stabilizing effect of the Ag atoms on the surface, and thus they do not represent a rate-limiting process (Fig. 3A).

The reaction sequence toward **3** is illustrated in Fig. 3B. The rate-determining first step involves two C^1–C^5 cyclizations of the sterically less hindered terminal enediynes to yield benzofulvene diradicals. The radicals localized on the exocyclic double bonds subsequently recombine in a formal C^1–C^4 cyclization to yield the four-membered ring in the transient intermediate **tInt1**. This process involves the formation of three new carbon-carbon bonds, yet it lacks the aromatic stabilization associated with the formation of the naphthyl fragment in **Int2** and is consequently less exothermic (–60.7 kcal mol^{-1}). A sequence of bond rotations transforms **tInt1** via **Int3** into **tInt2**. Alignment of the unsaturated carbon valences in diradical **tInt1** with underlying Ag atoms maximizes the interaction with the substrate and induces a highly nonplanar arrangement, thereby making subsequent rotations essentially barrierless. [1,2]-Hydrogen shifts and a formal C^1–C^6 cyclization yield the biphenylene **3**.

Both reaction pathways toward **2** and **3** involve C^1–C^5 enediyne cyclizations. These are generally energetically less favorable relative to the preferred C^1–C^6 Bergman cyclizations (*22*), but factors such as the steric congestion induced by substituents on the alkynes (*12*, *22*), the presence of metal catalysts (*26*), or single-electron reductions of enediynes (*27*, *28*) have been shown to sway the balance toward C^1–C^5 cyclizations yielding benzofulvene diradicals. All three of these factors apply to the present case of the thermally induced cyclization of **1** on Ag(100)